NJC

ROYAL SOCIETY OF CHEMISTRY

PAPER

View Article Online
View Journal | View Issue

Cite this: *New J. Chem.*, 2021, **45**, 1404

Hierarchically interconnected ZnO nanowires for low-temperature-operated reducing gas sensors: experimental and DFT studies†

Parameshwar R. Chikate, [a] Alfa Sharma, [a] Sachin R. Rondiya, [b] Russell W. Cross, [b] Nelson Y. Dzade, [b] Parasharam M. Shirage [a] and Rupesh S. Devan *[a]

The well-constituted hierarchical arrangement of hexagonal ZnO nanowires with diameters <180 nm and lengths ~5–6 μm with clearly visible textural boundaries provided a highly porous film of thickness, ~1300 nm over a large area. The ZnO nanowires delivered excellent sensing performance for CO, C_2H_5OH, and NH_3 reducing gases at a safe detection limit of 50 ppm at an operating temperature of 100 °C. A maximum response of 115% and the response and recovery time of 27 and 9 s, respectively, were recorded for toxic 50 ppm NH_3 gas at the operating temperature of 100 °C, which is better than the performance of various previously reported pristine and doped ZnO nanostructures. The experimental observations are corroborated by first-principles density functional theory (DFT) calculations, which were performed to determine the reactivity of gas molecules with hexagonal ZnO nanowires. The expedited sensing response is ascribed to the larger potential barrier offered by the well-interconnected hierarchical growth of hexagonal ZnO nanowires.

Received 24th October 2020,
Accepted 10th December 2020

DOI: 10.1039/d0nj05231k

rsc.li/njc

Introduction

In the recent era, smart technologies are necessitating advancement to address safety and security concerns on high priority. The enormous growth of industrialization for luxurious lifestyle has impaired human and environmental health owing to the exhaust of hazardous gases and chemical compounds. Moreover, the dangerous condition of global warming is demanding the early monitoring of air quality and the detection of toxic and explosive gases to control their detrimental effect on the human life and environmental health. The controlled monitoring of harmful gaseous byproducts is urgently required. The involvement of largely generated poisonous carbon monoxide in climate change and the detrimental influence of explosive ethanol (C_2H_5OH) and highly toxic ammonia (NH_3) on health call for immediate detection and monitoring. Nontoxic metal oxides, which deliver excellent electronic mobility along with thermal and chemical stability, are competent candidates to assist in this purpose; however, they suffer from poor selectivity and sensitivity for various gases. The gas sensing mechanism, which involves the gas–solid interaction at surfaces, can be improved by providing a large active surface area at nanoscale dimensions. Recent gas sensing approaches have shown that the sensing properties of metal oxides can be significantly enhanced by controlling the nanostructure surface morphologies.[1,2] The gas sensing performance of various metal oxides, such as SnO_2, In_2O_3, TiO_2, WO_3, α-Fe_2O_3, and ZnO, in diverse morphological forms has been investigated.[1–3] These metal oxides challenge researchers to improve sensing mechanisms due to their higher working temperature, low sensitivity, poor selectivity, short-term stability, and durability. However, ZnO, a widely explored n-type semiconductor with a large bandgap, greater electronic mobility, and ultimate chemical and thermal stability at the nanosize, shows good competency for further improvement in sensing ability.[4,5] Although the crystal structure, surface morphology, chemical composition, and operating temperature govern the sensing performance of ZnO nanostructures, doping metals such as Ag,[6] Al,[7] Co,[8] Cu,[9] Fe,[10] Mn,[11] Pd,[12] Pt,[13] and Ta[14] in ZnO was adopted to enhance electronic properties for improvement in the gas sensing performance. However, among all explored ZnO nanosize morphologies, one-dimensional (1D) nanostructures deliver large surface-to-volume ratios and continuous pathways for electron transfer,[3,15–17] which facilitate gas molecule adsorption and prompt electronic transportation in one dimension.

[a] *Department of Metallurgy Engineering & Materials Science, Indian Institute of Technology Indore, Simrol, Indore 453552, India. E-mail: rupesh@iiti.ac.in*
[b] *School of Chemistry, Cardiff University, Cardiff, CF10 3AT, Wales, UK*

† Electronic supplementary information (ESI) available. See DOI: 10.1039/d0nj05231k

The working temperature governs the reaction kinetics, conductivity, and electronic movements, which explicitly control the sensing activity of ZnO nanostructures.[18,19] Even though the surface redox reaction is activated at high temperature and enhances the reaction kinetics for sensing activity, ZnO nanostructures have shown prominent gas sensing performance at relatively high temperatures in the range from 300 °C to 500 °C.[20] These high working temperatures induce secondary grain growth, causing instability, inaccuracy, high power consumption, and lack of durability in the sensing mechanism. Therefore, reducing the operating temperature range of ZnO nanostructures is a critical challenge. Significant efforts to develop lower working temperature-based ZnO gas sensors are prerequisites in light of safety concerns related to these flammable and toxic gases. ZnO-based sensors have detected gases such as CO, NH_3, C_2H_5OH, NO_2, C_6H_6, and H_2S; however, prompt and high-sensing responses were achieved only at high working temperatures due to the thermal excitation-driven increase in the surface electrons. Despite the significant effect of the number of grains between interelectrode gaps on the responses of ZnO nanorods and nanoparticles, the maximum response for 50 ppm NO_2 gas (*i.e.*, 44.2) was observed at the temperature of 300 °C.[21] Moreover, the hierarchical hollow ZnO microspheres delivered a maximum response at a lower temperature of 275 °C for various C_2H_5OH concentrations (8 to 100 ppm).[22] Randomly aligned ZnO nanowires on a patterned ZnO:Ga/SiO_2/Si template delivered a maximum sensor response (22.5%) at 300 °C for 1000 ppm NH_3 gas, which improved further to 36% (@1000 ppm) after heavy loading of Pt nanoparticles.[23] Recently, Colak *et al.*[24] observed improvement in the CO_2 sensing ability of ZnO nanorods after doping Ge, Nd, and W in lower proportions. However, the maximum sensing response was still observed at a very high temperature of 450 °C. Moreover, the hierarchical ZnO nanostructures delivered better gas response (*i.e.* R_a/R_g = 177.1) for 100 ppm C_2H_5OH at 450 °C than at room temperature (*i.e.* R_a/R_g = 24.7).[25] However, to the best of our knowledge, ZnO nanostructures have yet to deliver the best performance at a temperature below 150 °C for sensing CO, C_2H_5OH, and NH_3 gases for possible applications in wearable sensors.

Therefore, here, we demonstrate the gas sensing performance of ZnO nanowires at lower operating temperatures. The comparative studies illustrate that the ZnO nanowires synthesized by a cost-effective hydrothermal technique delivered the best sensing performance for CO, C_2H_5OH, and NH_3 gases at a relatively low operating temperature of 100 °C. Sensor responses of 29%, 98%, and 115% were observed for CO, C_2H_5OH, and NH_3 gas, respectively, at the operating temperature of 100 °C. Furthermore, response and recovery times of 27 and 9 s were recorded for toxic NH_3 gas at the temperature of 100 °C, respectively, indicating the faster response of ZnO nanowires to NH_3 gas. Furthermore, the experimental observations were validated with electronic structure DFT calculations performed to systematically characterize the reactivities of CO, C_2H_5OH, and NH_3 gases towards the hexagonal ZnO nanowires.

Experimental

(a) Synthesis and characterization

The large area arrays of ZnO nanowires were synthesized using a hydrothermal technique. The reaction of zinc acetate dihydrate ($C_4H_6O_4Zn{\cdot}2H_2O$) and sodium peroxide (Na_2O_2) was carried out in an autoclave at an optimized temperature of 85 °C for 12 h to grow the ZnO nanowires over ITO-coated glass substrates hydrothermally. The synthesis protocol of the ZnO nanowires is akin to that reported in ref. 15. The surface morphological features of the ZnO nanowires were substantiated from field emission scanning electron microscopy (FESEM, JEOL, JSM 7610 F Plus). The crystal structure was analyzed using an X-ray diffractometer (D8 Advance, Bruker AXS) with Cu kα radiation (λ = 1.5405 Å) and a micro-Raman spectrometer (Renishaw InVia system) with 532 nm incident photons from a diode-pump solid-state laser operated at a minimum power of 17 mW. The chemical analysis of the ZnO nanowires was revealed from XPS. The gas-sensing performance of the ZnO nanowires was measured in a home-built setup.[26] The sensing measurements were performed after exposure to different amounts of reducing gases such as CO, C_2H_5OH, and NH_3 gases. Considering that gas adsorption and diffusion are thermally activated processes, the gas sensing performance of the ZnO nanowires was related to the sensing temperature to identify the optimal working/operational temperature. The sensing behavior was determined for various gas concentrations (*i.e.*, 10, 20, 50, 100 ppm) at different operation temperatures ranging from 30 °C (R.T.) to 150 °C by measuring the changes in the resistance of the ZnO nanowires in air and gas environments. The gas sensing response (S%) for the reducing gases was estimated from ref. 7 and 27.

$$S\ (\%) = (R_{air} - R_{gas})/R_{gas} \times 100 \quad (1)$$

where S (%) is the sensor response and R_{air} and R_{gas} are the resistance of the sensor material in the air and gas environments, respectively. The response and recovery times were estimated at 90% of the maximum and minimum resistance values observed for the ZnO nanowires, respectively, during gas sensing studies.[26]

We also observed variations in sensor resistance values in air when the ZnO sample was subjected to different temperatures from 30 °C to 150 °C. The changes in the resistance values of ZnO are provided in Table 1. These values are in kΩ; however, the resistance during the sensing performance is in MΩ. Therefore, this change in the resistance is not visible in the figures.

Table 1 The change in the resistance (kΩ) of ZnO in the different gas environments to air resistance

Operating temperature			
Gas	50 °C	100 °C	150 °C
NH_3	33	44	30
C_2H_5OH	128	1325	50
CO	47	182	7

(b) Computational analysis

The electronic structure density functional theory (DFT) calculations were performed using the Vienna *Ab initio* Simulation Package (VASP),[28] wherein the interactions between the core and valence electrons were treated using the Project Augmented Wave (PAW) method.[29] The electronic wave functions were expanded on a plane-wave basis set with a cutoff energy of 600 eV. Geometry optimizations were performed using the conjugate-gradient algorithm until the residual Hellmann–Feynman forces on all relaxed atoms reached 10^{-3} eV $Å^{-1}$. The electronic exchange–correlation potential was calculated using the Perdew–Burke–Ernzerhof (PBE) generalized gradient approximation (GGA) functional.[30] Long-range vdW interactions were accounted for using the method of the Grimme DFT-D3 scheme.[31] The bulk ZnO was modeled in the hexagonal wurtzite phase, and a $7 \times 7 \times 5$ Monkhorst–Pack *k*-point mesh was used to sample the Brillouin zone. The screened hybrid functional HSE06[32] was used with an exchange value of 25% to predict the bandgap accurately. The $(10\bar{1}0)$ surface is generally predicted to be the most stable surface of ZnO,[33,34] and it is expected to be the most expressed and abundant facet in ZnO nanocrystals. The ZnO $(10\bar{1}0)$ surface has been used in previous studies to characterize the interactions of NO_2, NO, O, and N species. Therefore, the ZnO $(10\bar{1}0)$ surface was preferred in the present study to describe the adsorption reactions of CO, C_2H_5OH, and NH_3 gas molecules. METADISE code[35] was utilized to ensure the creation of non-dipolar stoichiometric surfaces from optimized bulk wurtzite ZnO.[36] The ZnO $(10\bar{1}0)$ surface used to characterize the adsorption reactions of CO, C_2H_5OH, and NH_3 gas molecules was created from the optimized bulk ZnO using METADISE code,[35] which ensures the creation of a surface with a zero dipole moment perpendicular to the surface plane. The gas molecule adsorption calculations were carried out on a ZnO$(10\bar{1}0)$–(3×3) surface coverage, which is large enough to minimize lateral interactions between the molecules in neighboring image cells. No symmetry constraints were imposed on the structural optimization of the gas–ZnO$(10\bar{1}0)$–(3×3) systems, and in particular, the molecules were free to move away laterally and vertically from their initial binding sites or reorient themselves to find the lowest-energy adsorption configuration. A $3 \times 3 \times 1$ *k*-point was used for the surface calculations. Bader charge analysis[37] was used to quantify any charge transfers between the ZnO$(10\bar{1}0)$ surface and the gas molecules.

Results and discussion

Fig. 1(a) illustrates the FESEM image of the surface morphology of the large-area arrays of ZnO nanowires grown on ITO-coated glass substrates. The high-magnification FESEM image in the inset of Fig. 1(a) (and Fig. S1 in the ESI†) confirms that all the hexagonal ZnO nanowires with clearly visible textural boundaries are confined to diameters of <180 nm and lengths of $\sim$5–6 μm. The well-constituted hierarchical arrangement of ZnO nanowires provided a highly porous $\sim$1300 nm thick film over a large area.

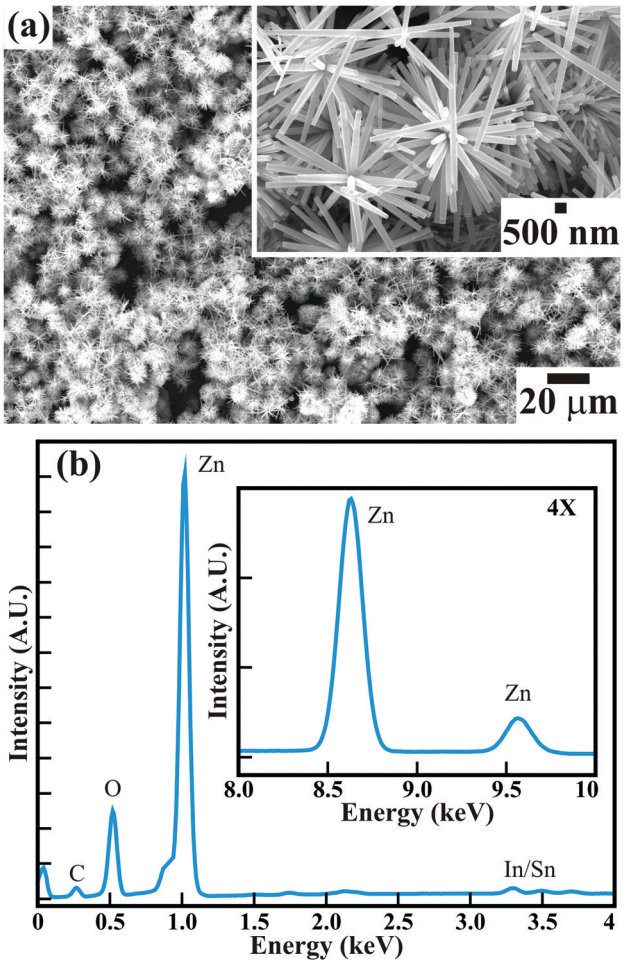

Fig. 1 (a) FESEM image and (b) EDS of large-area arrays of ZnO nanowires grown on ITO-coated glass substrates. The high-magnification FESEM image in the inset of (a) shows the hierarchical growth of the ZnO nanowires.

The surface morphological appearance of the hexagonal ZnO nanowires is detailed elsewhere.[15] The highly porous thin film of single-crystalline ZnO nanowires is expected to provide distinct gas sensing properties. The energy dispersive X-ray (EDX) spectra of the ZnO nanowires (Fig. 1(b)) corroborates the presence of Zn and O elements in the array of hexagonal ZnO nanowires. The presence of In and Sn is confirmed with small peaks. Moreover, the presence of a relatively very small peak of C confirms the presence of a negligible amount of C over the surface of the ZnO nanowires array. X-ray photoelectron spectroscopy (XPS) confirmed the formation of stoichiometric ZnO nanowires. The XPS analysis (not provided here) is very much akin to that in our studies reported earlier.[15] The phase purity and crystal structure of the as-synthesised ZnO nanowires analyzed from X-ray diffraction (XRD) studies (ESI†) confirmed the growth of hexagonal wurtzite ZnO nanowires without any defects or impurity phases. Therefore, the present hexagonal ZnO nanowires with a high degree of crystallinity were expected to enable better sensing response for hazardous and toxic gases such as CO, C_2H_5OH, NH_3, *etc.*

Raman scattering was performed at room temperature to investigate the vibrational properties of the ZnO nanowires. Fig. 2 shows five prominent Raman active bands, which are A_1 + E_1 + $2E_2$ Raman active modes as explained by group theory, where A_1 and E_1 are the Raman and infrared active polar modes and E_2 is the Raman active nonpolar mode. The Raman bands observed at 328, 373, 431, 530, and 576 cm^{-1} are assigned to the A_1, A_1, E_2, A_1, and E_1 modes of wurtzite ZnO, respectively.[38–40] The peak around 373 cm^{-1} is ascribed to the transverse optical A_1 mode resulted from the polarized A_1 and E_1 modes of the vibrations. A highly intense Raman band at 431 cm^{-1} is assigned to the high crystallinity of the hexagonal ZnO nanowires array.[41] The Raman band at 576 cm^{-1} corresponds to the E_1 mode for the presence of oxygen vacancies and interstitial oxygen as well as the complexes of Zn.[42] However, the relatively low intensity indicates that the ZnO nanowires exhibit a smaller amount of oxygen vacancies. Moreover, the red shifting of the Raman bands in the ZnO nanowires (Table S1, ESI†) compared to those of other reported nanostructure morphologies and the bulk wurtzite structure of ZnO indicate phonon confinement. This reconfirms that the hexagonal wurtzite ZnO nanowires grown on ITO-coated glass substrates are highly crystalline with the lower amount of oxygen deficiencies.

The temperature-dependent sensing performance of the ZnO nanowire arrays was performed for various concentrations of CO, C_2H_5OH, and NH_3 reducing gases. The optimized gas sensing performance was confirmed in resistive mode. Fig. 3 shows the temperature-dependent real-time dynamic resistance response transients of the ZnO nanowires for 10 to 100 ppm of CO. Sequential exposure of 10, 20, 50, and 100 ppm CO to ZnO nanowires maintained at room temperature (*i.e.*, 30 °C) confirmed the cyclic variation in the resistance. A similar trend was observed in the resistance variation when the ZnO nanowires were maintained at temperatures of 50 °C, 100 °C, and 150 °C. The resistance of the ZnO nanowires was reduced with increasing CO concentration and was further altered with temperature variation. Fig. 3(b) illustrates the influence of temperature and CO concentration on the sensing response of the ZnO nanowires. The sensing response of the ZnO nanowires improved with increasing concentration of CO from 10 to 100 ppm for all studied temperatures. Even though the best response was observed for 100 ppm, the most compelling response was estimated for the 20 ppm CO. The best responses of 17.4%, 23.6%, 31.6%, and 28.3% were observed for 100 ppm CO, and relatively compelling responses of 11.5%, 13.7%, 30.3%, and 20.2% were observed for 20 ppm CO when the ZnO nanowires were maintained at temperatures of 30 °C, 50 °C, 100 °C and 150 °C, respectively. However, the temperature-influenced sensing response was effective for all the concentrations of CO. The response improved with increasing temperature and was reduced at higher temperatures beyond 150 °C after achieving the maximum response at 100 °C (Fig. 3(b)). A fitted logarithmic plot between the response (*S*%) and gas concentration (Fig. 3(c)) illustrates the gas detection limit of the ZnO nanowires. The estimated detection limit for CO shows a progressive decrease of 3.57, 1.07, 1, and 1.02 ppm with increasing operating temperature from 30 °C to 150 °C, respectively.[43] The highest responses of 26.2%, 30.3%, 31.9%, and 31.6% were observed for 10, 20, 50, and 100 ppm CO (Fig. 3(d)), respectively, at a temperature of 100 °C. The saturation of the adsorption and desorption reaction processes may have resulted in the steady response above 50 ppm. The response and recovery times estimated at 100 °C were 25.0 and 17.5 s for 50 ppm CO and 15.1 and 12.5 s for 100 ppm CO, which are superior (Table S2, ESI†). Furthermore, the ZnO nanowires showed better sensing response at 100 °C for 50 ppm CO by delivering a maximum response of 31.9%. The hexagonal ZnO nanowires exhibited excellent and faster response within the detection safety limit for CO (*i.e.*, ~50 ppm) at relatively very low temperatures compared to the pristine and metal-doped ZnO nanostructures, as listed in Table S3 (ESI†).

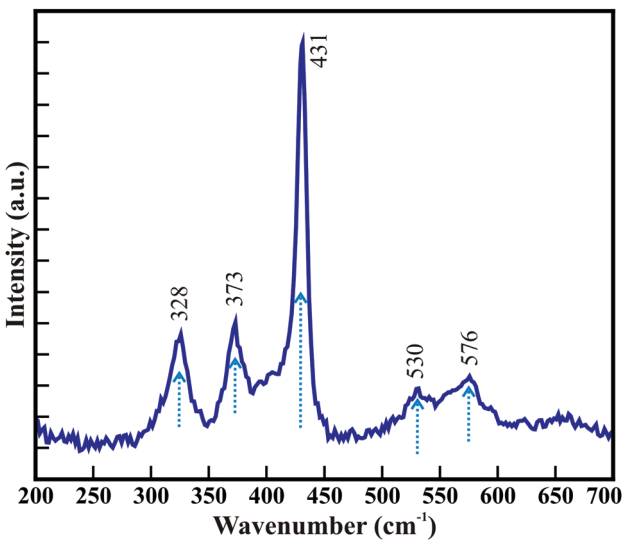

Fig. 2 Raman spectra of hexagonal ZnO nanowires.

Likewise, Fig. 4 shows the temperature-dependent real-time dynamic resistance response transients of the ZnO nanowires for 10 to 100 ppm of C_2H_5OH. A sequential assortment of 10, 20, 50, and 100 ppm C_2H_5OH at room temperature (*i.e.*, 30 °C) confirmed the cyclic variation in the resistance, akin to that observed for CO gas. Similar behavior was observed at 50 °C, 100 °C, and 150 °C. The resistance of the ZnO nanowires was reduced with increasing concentration of C_2H_5OH and was further altered after varying the temperature. Fig. 4(b) illustrates the influence of temperature and C_2H_5OH concentration on the sensing response of the ZnO nanowires. The sensing response is influenced remarkably by the temperature for all concentrations of C_2H_5OH studied. The response improved with increasing temperature but decreased for higher temperatures (*i.e.*, 150 °C) after achieving a maximum response at 100 °C for all the C_2H_5OH concentrations. The best sensing response for all the concentrations of C_2H_5OH was observed at the temperature of 100 °C. Response values of 55.7%, 63.2%, 101.9%, and 82.8% were observed for 10, 20, 50, and 100 ppm C_2H_5OH, respectively, at the temperature of 100 °C. The sensing response of the ZnO nanowires improved with increasing concentration of C_2H_5OH.

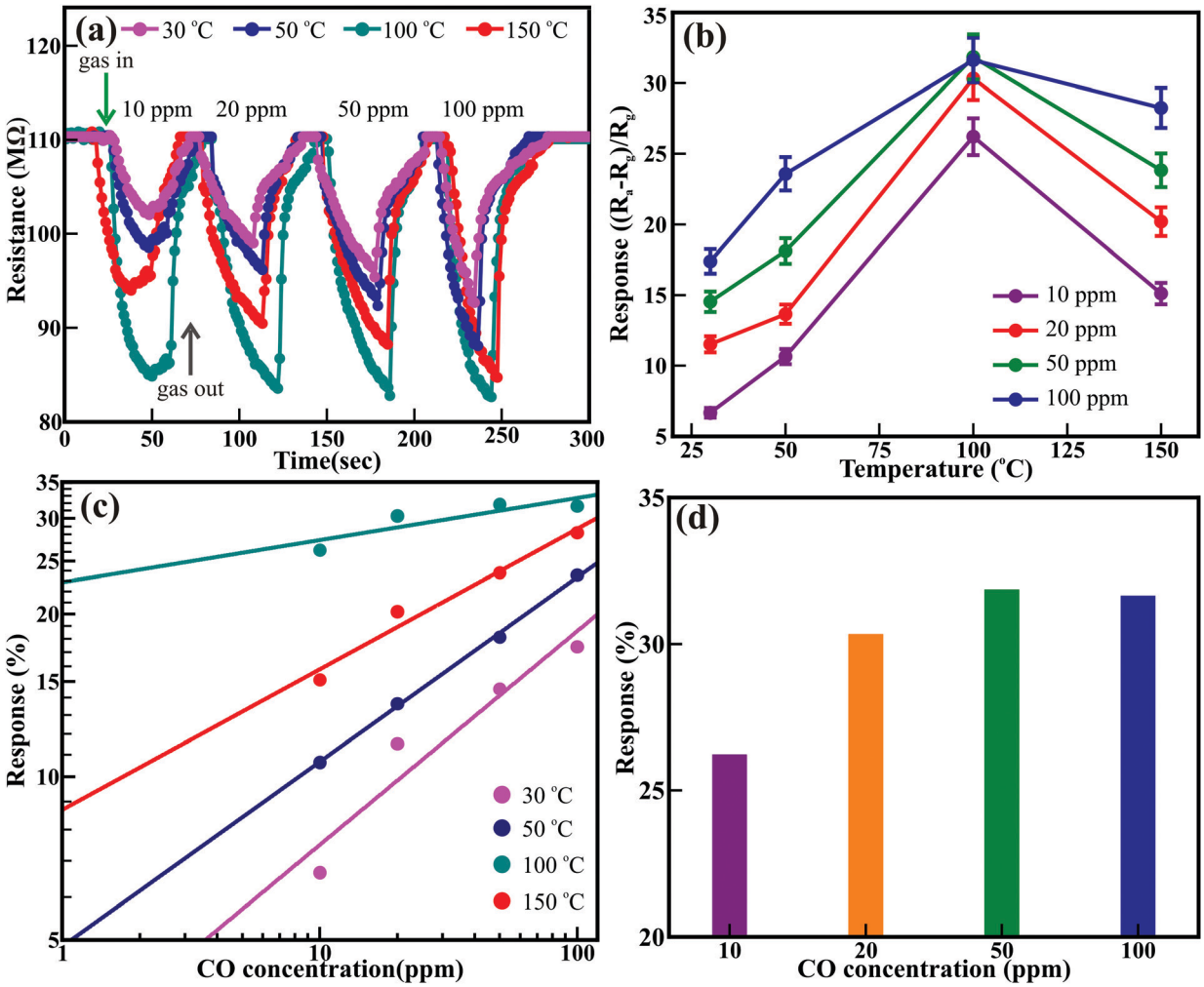

Fig. 3 (a) Time-dependent response–recovery behavior of ZnO nanowires with different concentrations of CO gas at various operating temperatures (*i.e.*, 30 °C, 50 °C, 100 °C and 150 °C). (b) Temperature-dependent response behavior of ZnO nanowires with different concentrations of CO gas. (c) CO concentration-dependent response behavior of ZnO nanowires at different operating temperatures. (d) The optimum sensing response of the ZnO nanowires sensor as a function of CO concentration at the operating temperature of 100 °C.

The highest sensing responses of 58.4%, 73.7%, 101.9%, and 86.9% were observed at the temperatures of 30 °C, 50 °C, 100 °C, and 150 °C, respectively, after exposing the ZnO nanowires to 50 ppm C_2H_5OH. The reason for the reduction in the response at higher temperature (>100 °C) is not well understood; however, the saturation of adsorption and faster desorption reaction processes may be the origin of this effect. The detection limit of the ZnO nanowire sensor for C_2H_5OH gas was estimated from the linear fitting of the log–log plot of the response and gas concentration, as shown in Fig. 4(c). Detection limits of 4.98, 1.34, 1.01, and 1.02 ppm were observed as the operating temperature increased from 30 °C to 150 °C, respectively. Moreover, the response and recovery times estimated for 50 ppm C_2H_5OH at 100 °C are 40.3 and 19.4 s., respectively, which are relatively more significant than those of ZnO nanorods (53 and 48 s for 50 ppm at 340 °C).[44] Overall, the ZnO nanowires showed better sensitivity at 100 °C for the 50 ppm C_2H_5OH by delivering a maximum response of 101.9% (Fig. 4(d)). This sensing response of ZnO nanowires is very high at a relatively low temperature compared to the responses of pristine, doped, and decorated ZnO nanostructures, as listed in Table S4 (ESI†). Moreover, the ZnO nanowires delivered better responses than the values reported by Guo *et al.*[45] for ZnO nanowires (*i.e.*, 3.7% at 380 °C), which achieved a value of 33.6% (@380 °C) after functionalization with Au nanoparticles.[48] Wang *et al.* reported that hydrothermally synthesized ZnO nanorods provided a maximum response of ~22% for 50 ppm at 320 °C but did not respond below 200 °C.[44] Although Al-doped ZnO nanostructures embedded in multi-microstructures delivered a sensing response of ~40% at 160 °C, the exceptionally high exposure of 3000 ppm C_2H_5OH played a significant role and strongly influenced this gain.[46]

Subsequently, the ZnO nanowires arrays were subjected to NH_3 gas sensing. Fig. 5 shows the real-time dynamic resistance response transients of the ZnO nanowires in a controlled NH_3 atmosphere (*i.e.*, 10 to 100 ppm) at various temperatures. Sequential exposure to 10, 20, 50, and 100 ppm NH_3 gas atmosphere at room temperature (*i.e.*, 30 °C) confirmed distinct

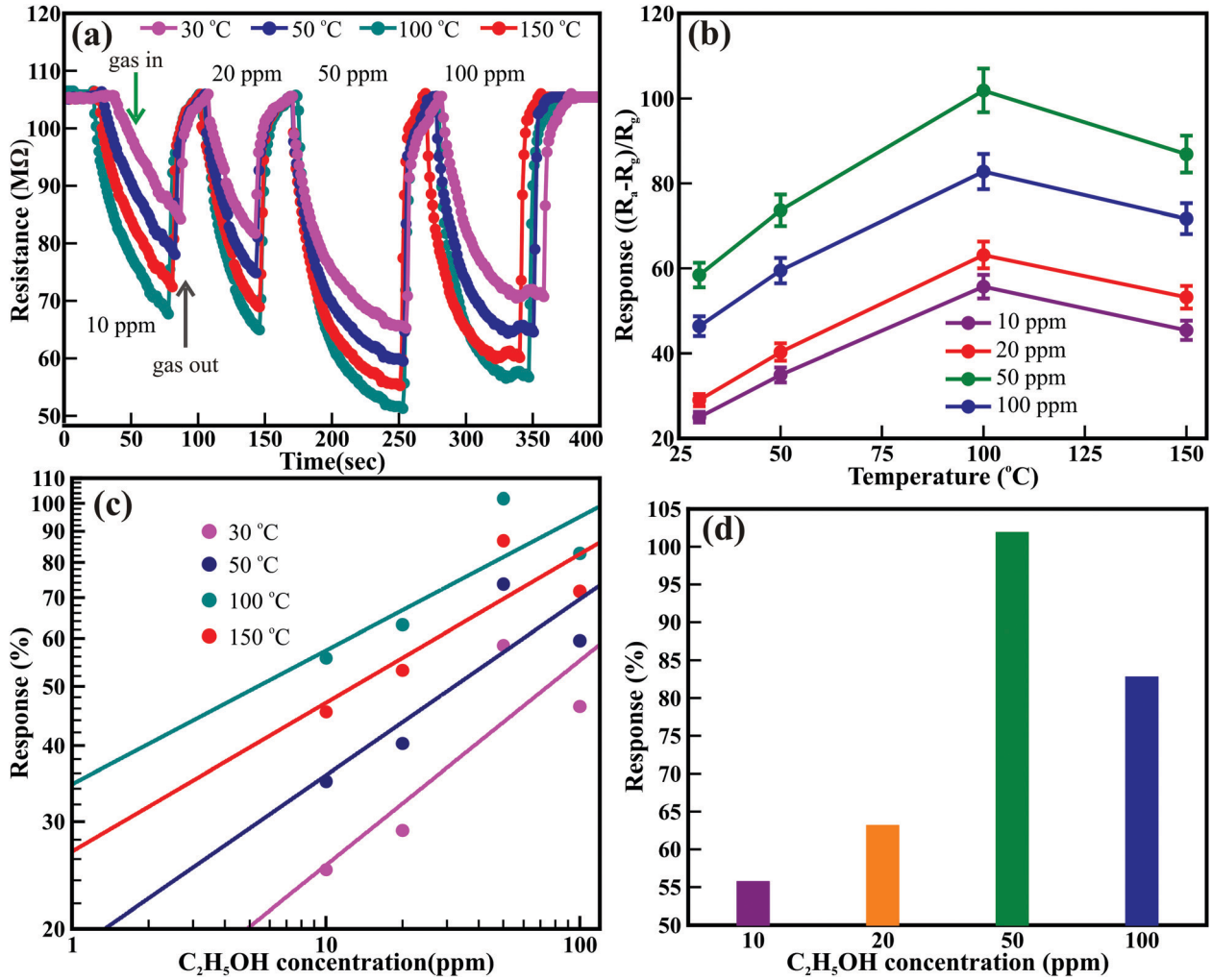

Fig. 4 (a) Time-dependent response–recovery behavior of ZnO nanowires with different concentrations of C_2H_5OH gas at various operating temperatures (*i.e.*, 30 °C, 50 °C, 100 °C and 150 °C). (b) Temperature-dependent response behavior of ZnO nanowires with different concentrations of C_2H_5OH gas. (c) C_2H_5OH concentration-dependent response behavior of ZnO nanowires at different operating temperatures. (d) The optimum sensing response of the ZnO nanowires sensor as a function of C_2H_5OH concentration at the operating temperature of 100 °C.

variations in the resistance (Fig. 5(a)) akin to those observed for C_2H_5OH and CO gases. The resistance of the ZnO nanowires was reduced with increasing NH_3 gas concentration. A similar trend was observed for 50 °C, 100 °C, and 150 °C in addition to the significant decrease in the resistance with changing temperature. Fig. 5(b) illustrates the effects of the temperature and concentration of NH_3 gas on the sensing performance of the ZnO nanowires. The sensing response is influenced by temperature irrespective of the variation in the concentration of NH_3. The response was enhanced with increasing temperature but decreased after achieving the maximum response at 100 °C for all the concentrations. The best responses of 105.5%, 109.7%, 115.9%, and 128.9% were observed for 10, 20, 50, and 100 ppm NH_3, respectively, at a constant temperature of 100 °C. Moreover, the sensing response increased with increasing NH_3 concentration irrespective of temperature. Higher sensing responses of 71.0%, 85.7%, 128.9%, and 103.5% were observed after exposing the ZnO nanowires to 100 ppm NH_3 at temperatures of 30, 50, 100, and 150 °C, respectively. However, the ZnO nanowires showed excellent response at 100 °C irrespective of the concentration of NH_3. The maximum responses of 115.9% and 128.9% were observed at 100 °C for 50 and 100 ppm NH_3, respectively (Fig. 5(d)). Detection limits of 5.93, 1.02, 1.01, and 1.02 ppm were estimated for NH_3 gas at the operating temperatures of 30, 50, 100, and 150 °C, respectively (Fig. 5(c)). The estimated response and recovery times at 100 °C were 18.3 and 10.8 s for 50 ppm NH_3 and 20.7 and 13.5 s and 100 ppm NH_3 which are better than those of various ZnO nanostructures reported in the literature (Table S5, ESI†). This confirms that the ZnO nanowires deliver a faster response to NH_3 than to C_2H_5OH and CO gases. Moreover, the hexagonal ZnO nanowires delivered excellent response to NH_3 gas at a lower temperature (*i.e.*, 100 °C) than those of the various pristine and metal-doped ZnO nanostructures mentioned in Table S6 (ESI†). Recently, Tharsika *et al.*[47] revealed a sensing response of 285% toward 400 ppm NH_3 at 400 °C for ZnO

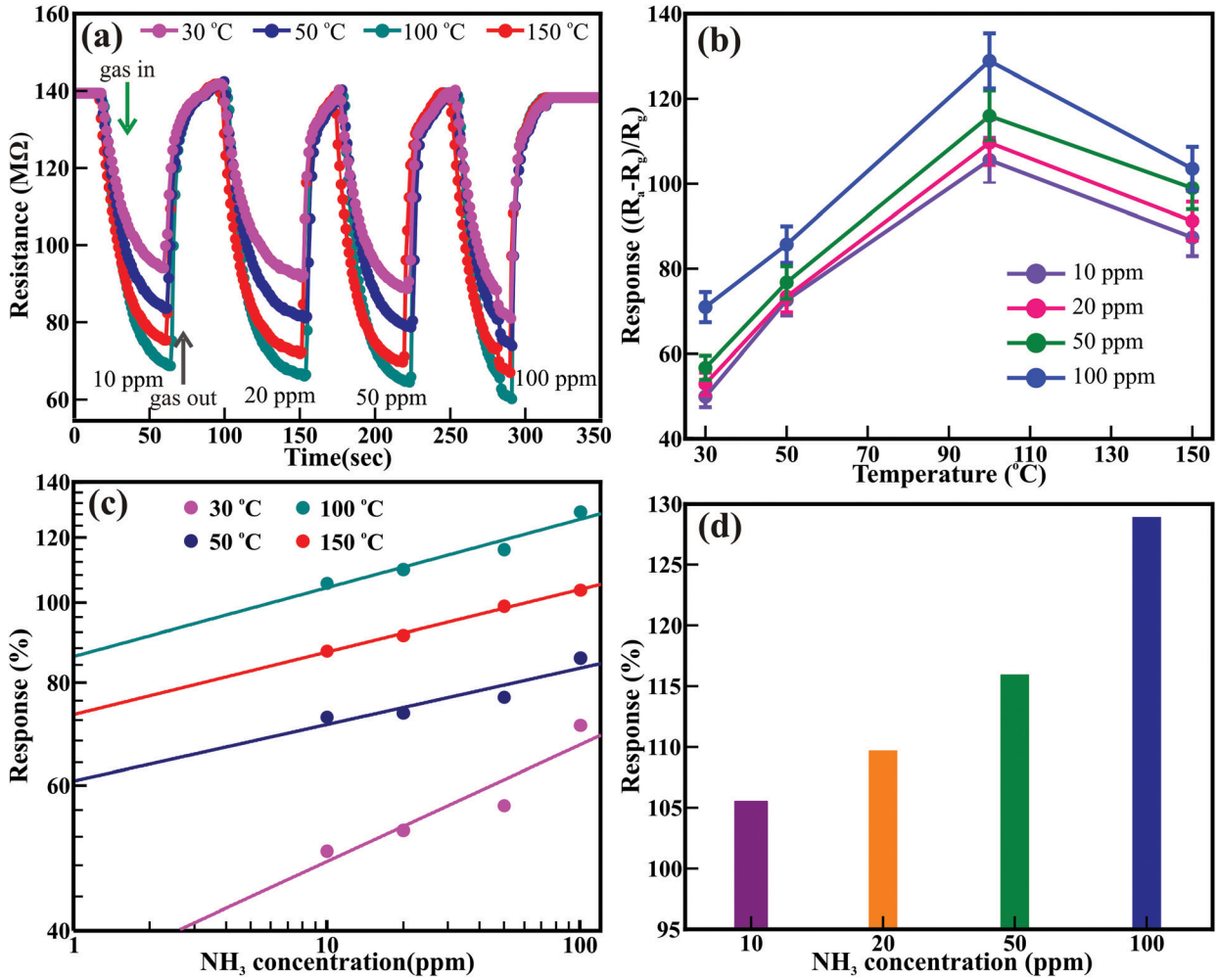

Fig. 5 (a) Time-dependent response–recovery behavior of ZnO nanowires with different concentrations of NH_3 gas at various operating temperatures (*i.e.*, 30, 50, 100 and 150 °C). (b) Temperature-dependent response behavior of ZnO nanowires with different concentrations of NH_3 gas. (c) NH_3 concentration-dependent response behavior of ZnO nanowires at different operating temperatures. (d) The optimum sensing response of the ZnO nanowires sensor as a function of NH_3 concentration at the operating temperature of 100 °C.

nanorods deposited over SnO_2 thin film; however, reduction in the concentration of NH_3 enormously reduced the response. Li *et al.*[47] reported a sensor response of 57.5% for 600 ppm NH_3 at 150 °C using ZnO nanoparticles; however, the response was reduced to 18% for 50 ppm.

Fig. 6 presents the histogram of the most effective sensing performance (Fig. 6(a)) and selectivity performance (Fig. 6(b)) of the ZnO nanowires at the optimal working temperature of 100 °C for the CO, C_2H_5OH, and NH_3 gases. The selectivity of a sensor describes its ability to differentiate a specific target gas from other interfering gases. The selectivity parameter (β) is generally defined as[48] $\beta = S_{\text{interfering}}/S_{\text{target}}$, where S_{target} and $S_{\text{interfering}}$ are the response of the target gas (NH_3) and other gases (CO and C_2H_5OH), respectively. The estimated selectivity parameter is shown in Fig. 6(b). The value of β lies within the 0.24–0.88 range, where maximum values of 0.88 and 0.27 were obtained for 50 ppm concentrations of C_2H_5OH and CO gases, respectively, at the optimum temperature of 100 °C. The hexagonal ZnO nanowires delivered the best response for the detection safety limit (*i.e.*, ~50 ppm) of all the studied gases at 100 °C, assigned to the deactivation of desorption and diffusion reaction processing, and inefficient adsorption and faster desorption below and above 100 °C, respectively.[50] Moreover, the adsorption and desorption of the oxygen species transformed the resistance of the ZnO nanowires with increasing temperature and dramatically controlled the response. Pristine ZnO nanostructures seldom offer perfect NH_3 sensing performance, except at higher temperatures. Although a few studies have reported the sensing response of ZnO to NH_3, a suitable response was obtained either at higher temperatures or after doping with metals (Table S6, ESI†). The ZnO nanowires in the present work delivered the highest response to NH_3 at 100 °C, which can be attributed to the well-defined hexagonal morphology, clearly visible textural boundaries, single-crystalline nature, and good interconnections of the nanowires owing to their hierarchical arrangement.

To gain further atomic-level insights into the gas sensing response of the ZnO nanowires, we performed first-principles

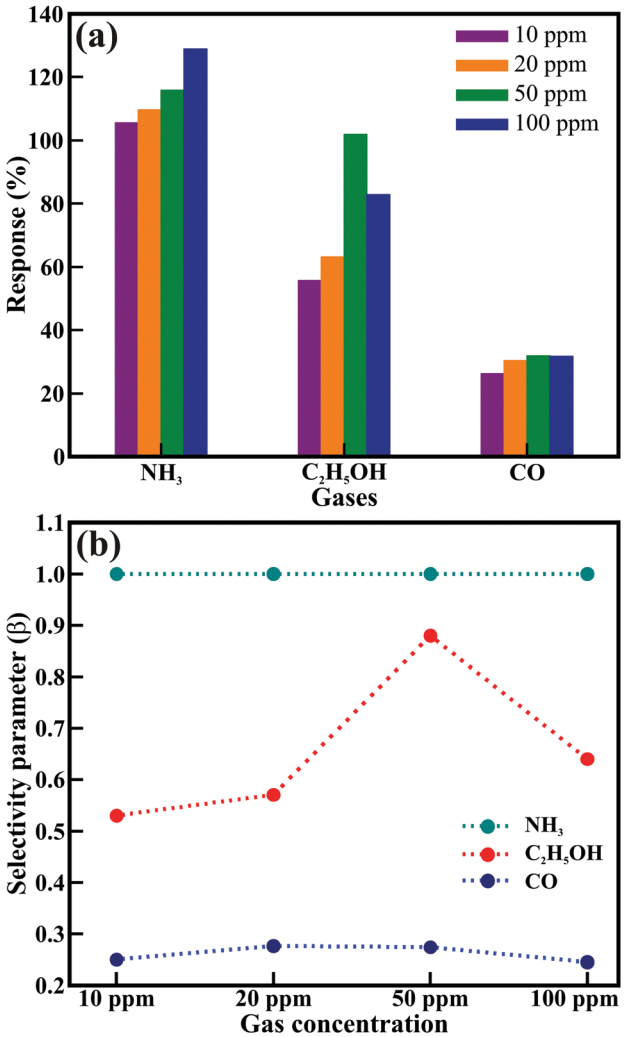

Fig. 6 (a) Histogram of the maximum sensor response and (b) variations in the selectivity parameter (β) of the ZnO nanowires sensor for 50 ppm CO, C_2H_5OH, and NH_3 gases at an operating temperature of 100 °C.

DFT simulations of the adsorption reactions between CO, C_2H_5OH, and NH_3 molecules and the ZnO $(10\bar{1}0)$ surface. Before investigating the adsorption reactions, the bulk ZnO was modeled in the hexagonal wurtzite phase with space group *P*63*mc* (no. 186), as shown in Fig. 7(a). The fully optimized lattice parameters predicted of $a = b = 3.275$ Å and $c = 5.284$ Å were in excellent agreement with experimentally observed lattice parameters. The partial density of states (Fig. 7(b)) reveals that the valence and conduction band edges are dominated by the O(2p) states with a small contribution from the Zn(3d) states. The bandgap of 3.24 eV predicted from the screened hybrid HSE06 functional[51] is consistent with experimentally reported values for ZnO.[4] Considering the key role of surface oxygen species in the gas response process over the ZnO surface, the adsorption of oxygen molecules on ZnO$(10\bar{1}0)$ surface was first explored and was found to preferentially adsorb dissociatively, as shown in Fig. 7(c). The Bader population shows that the dissociated O atoms gained 0.87 e^- each from the interacting surface Zn sites, resulting in the formation of $2O^-$ species. The adsorption energy (E_{ads}) of the gas molecules, which gives a measure of the strength of the gas–ZnO interactions, was calculated as $E_{ads} = E_{surf+gas} - (E_{surf} + E_{gas})$, where $E_{surf+gas}$ is the total energy of the surface and gas system in the equilibrium state, E_{surf} is the total energy of the isolated oxygen-covered O_2/ZnO$(10\bar{1}0)$ surface and E_{gas} is the total energy of the isolated gas molecules. Accordingly, a negative value of E_{ads} indicates exothermic and stable adsorption, whereas a positive value indicates unstable adsorption. The lowest-energy adsorption configurations of CO, C_2H_5OH, and NH_3 gas molecules are shown in Fig. 7(d–f). The CO molecule released the least adsorption energy of −1.35 eV compared to C_2H_5OH and NH_3, which released adsorption energies of −1.87 and −2.11 eV, respectively; this indicates that the order of the binding strength is CO < C_2H_5OH < NH_3. The stronger binding of NH_3 is consistent with the observed higher maximum response from the ZnO nanowires. From the Bader charge analyses, the adsorption of CO, C_2H_5OH, and NH_3 on the O_2/ZnO$(10\bar{1}0)$ surface demonstrate that the CO molecule acts as a charge acceptor, withdrawing 0.58 e^- from the surface after adsorption, whereas the C_2H_5OH and NH_3 molecules act as charge donors, transferring approximately 0.02 and 0.08 e^- per gas molecule to the surface.

The gas sensing mechanism is a surface-dependent property; however, it is determined by the change in the electrical properties of the sensor materials after exposure to the test gas environments. The resistance showed inverse behavior with temperature for n-type metal oxides; however, for ZnO, the adsorbed oxygen molecule is transferred to oxygen ions such as O_2^- (below 100 °C) O^- (100 °C to 300 °C) and O^{2-} (above 300 °C) by extracting free electrons at a certain temperature, which leads to an increase in the resistance.[6,11,12,49,52,53] The adsorption of oxygen molecules arrests the conduction bond electrons and also reduces the density of conduction, forming a depletion layer on the surface of the ZnO nanowires. After that, the depletion layer obstructs the charge carrier transportation and leads to a change in the resistance of the ZnO nanowires. The following equations explain this process of oxygen ion formation:

$$O_2(ads) + e^- \rightarrow O_2^-(ads) \quad (2)$$

$$O_2(ads) + 2e^- \rightarrow 2O^-(ads) \quad (3)$$

$$O^-(ads) + e^- \rightarrow O^{2-}(ads) \quad (4)$$

When reductive gases such as CO, C_2H_5OH, and NH_3 are introduced into the chamber, the amount of gas adsorption and the reaction rate increase with increasing temperature. However, the gas adsorption rate becomes close to the gas-desorption rate at 100 °C and delivers maximum sensor response. Above 100 °C, the reduced sensor response indicates a decrease in the quantitative adsorption of gases. Hence, the possible gas reaction with changes in the resistance of the hexagonal ZnO nanowires are as follows:[52,53]

$$CO + O_{ads}^- \rightarrow CO_2(gas) + e^- \quad (5)$$

$$C_2H_5OH + 6O^- \rightarrow 2CO_2 + 3H_2O + 6e^- \quad (6)$$

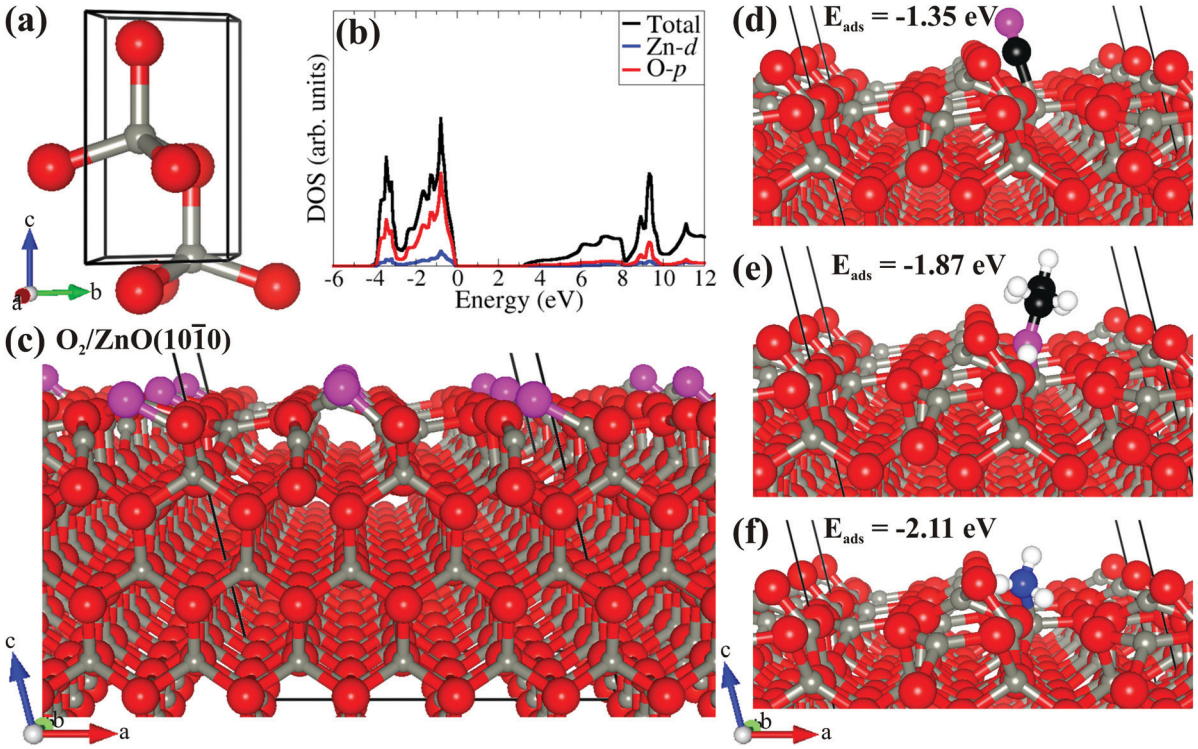

Fig. 7 Ball and stick models of (a) optimized hexagonal wurtzite bulk ZnO and (b) the corresponding partial density of states (PDOS); (c) surface structure of oxygen-covered (pink atoms) $O_2/(10\bar{1}0)$–(3×3); (d–f) lowest-energy adsorption structures of CO, C_2H_5OH, and NH_3, respectively. Colour code: light grey = Zn; red = O; black = C; blue = N; white = H, pink = O_{mol}.

$$2NH_3 + 3O^- \rightarrow 3H_2O + N_2 + 3e^- \quad (7)$$

Thus, NH_3 reacts with adsorbed oxygen ions along the surface of the ZnO nanowires after exposure, which releases the captured electrons and results in decreases in the potential barrier and thickness of the space-charge layer. This consecutively decreases the resistance; hence, the gas sensing performance increases (ESI†). Furthermore, the reducing NH_3 gas influences the width of the space charge region by discharging extra electrons during the interaction, thus decreasing the resistance.[6]

This phenomenon largely depends on the total surface area accessible for the interaction of gas molecules and is expedited by textural (or grain) boundaries contributing a resistive barrier. The high resistance in the present hexagonal ZnO nanowires array is assigned to its larger number of grain boundaries and contacts established between the ZnO nanowires. The corresponding schematic is shown in Fig. 8. Vertically grown individual nanowires (left panel, Fig. 8) have a restricted total surface area and potential barriers (*i.e.*, grain boundaries and point contacts). Therefore, most of the electrons from the ZnO nanowires directly flow with ease to the electrode. However, the hierarchically arranged ZnO nanowires (right panel, Fig. 8) furnished a much larger surface area and more potential barriers (*i.e.*, grain boundaries and point contacts). Most of the electrons need to flow across the grain boundaries and transfer through the point contacts established in the hierarchical arrangement. Hence, the electrons suffer a larger barrier before reaching the electrode, expediting the gas sensing

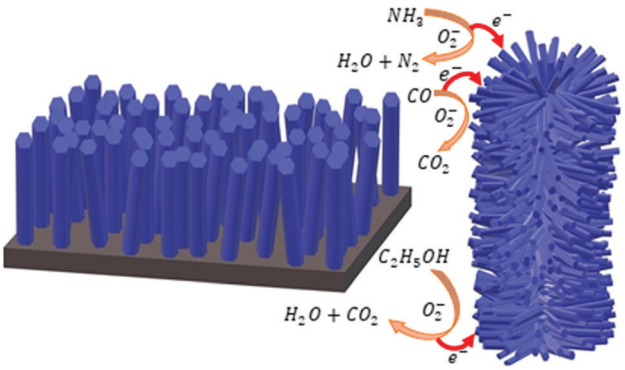

Fig. 8 Schematic representing the sensing mechanisms of vertically grown ZnO nanorods (left panel) and hierarchically grown ZnO nanowires (right panel).

mechanism. As a result, the present ZnO nanowires provided a higher response at a lower temperature than the various ZnO nanostructures reported in the literature.

Conclusions

In conclusion, hierarchical ZnO nanowires demonstrated excellent sensing performance for toxic gases. The ZnO nanowires delivered excellent sensing performance at the detection safety limits of 50 ppm for CO, C_2H_5OH, and NH_3 gases at a relatively

low operating temperature of 100 °C. The ZnO nanowires provided a maximum sensing response of 115 C_2H_5OH was observed at the temperature of 100% for toxic NH_3 gas and also delivered faster response and recovery times of 27 and 9 s, respectively, for 50 ppm NH_3 at the temperature of 100 °C, which are better than those of the variety of pristine, defect-controlled, and doped ZnO nanostructures. The complementary DFT analysis predicted the CO < C_2H_5OH < NH_3 order of the binding strength of the gas molecules. The excellent sensing response of the hierarchical hexagonal ZnO nanowires is ascribed to the well-defined hexagonal morphology, clearly visible textural boundaries, single-crystalline nature, and good interconnections of the nanowires. The sensing performance can be further improved after forming tunable hetero-architectures with metal nanoparticles.

Conflicts of interest

There are no conflicts to declare.

Acknowledgements

The authors are thankful to the UGC-DAE CSR Indore for their financial support of this research under grant no. CSR-IC-BL-65/CRS-182/2017-18/189. R. S. D. and N. Y. D. acknowledge the AESM, DUO-India Professor Fellowship award for this work. SRR, RWC, and NYD acknowledge the UK Engineering and Physical Sciences Research Council (EPSRC) for funding (Grant No. EP/S001395/1). This work has also used the computational facilities of the Advanced Research Computing, Cardiff (ARCCA) Division at Cardiff University and HPC Wales. This work also utilize the facilities of ARCHER (http://www.archer.ac.uk), the UK's national supercomputing service *via* the membership of the HEC Materials Chemistry Consortium funded by EPSRC (EP/L000202).

Notes and references

1 H. Zhang, W. G. Chen, Y. Q. Li and Z. H. Song, *Front. Chem.*, 2018, **6**, 7.
2 L. Zhu and W. Zeng, *Sens. Actuators, A*, 2017, **267**, 242–261.
3 R. S. Devan, R. A. Patil, J. H. Lin and Y. R. Ma, *Adv. Funct. Mater.*, 2012, **22**, 3326–3370.
4 J. H. Lin, R. A. Patil, R. S. Devan, Z. A. Liu, Y. P. Wang, C. H. Ho, Y. Liou and Y. R. Ma, *Sci. Rep.*, 2014, **4**, 6967.
5 R. S. Devan, J. H. Lin, Y. J. Huang, C. C. Yang, S. Y. Wu, Y. Liou and Y. R. Ma, *Nanoscale*, 2011, **3**, 4339–4345.
6 R. S. Ganesh, M. Navaneethan, V. L. Patil, S. Ponnusamy, C. Muthamizhchelvan, S. Kawasaki, P. S. Patil and Y. Hayakawa, *Sens. Actuators, B*, 2018, **255**, 672–683.
7 C. Y. Chi, H. I. Chen, W. C. Chen and C. H. Chang, *Sens. Actuators, B*, 2018, **255**, 3017–3024.
8 Y. J. Li, K. M. Li, C. Y. Wang, C. I. Kuo and L. J. Chen, *Sens. Actuators, B*, 2012, **161**, 734–739.
9 R. S. Ganesh, E. Durgadevi, M. Navaneethan, V. L. Patil, S. Ponnusamy, C. Muthamizhchelvan, S. Kawasaki, P. S. Patil and Y. Hayakawa, *Sens. Actuators, A*, 2018, **269**, 331–341.
10 G. S. T. Rao and D. T. Rao, *Sens. Actuators, B*, 1999, **55**, 166–169.
11 R. S. Ganesh, E. Durgadevi, M. Navaneethan, V. L. Patil, S. Ponnusamy, C. Muthamizhchelvan, S. Kawasaki, P. S. Patil and Y. Hayakawa, *J. Alloys Compd.*, 2017, **721**, 182–190.
12 P. Cao, Z. Yang, S. T. Navale, S. Han, X. Liu, W. Liu, Y. Lu, F. J. Stadler and D. Zhu, *Sens. Actuators, B*, 2019, **298**, 126850.
13 Y. Wang, X. N. Meng and J. L. Cao, *J. Hazard. Mater.*, 2020, **381**, 120944.
14 X. Huang, C. P. Li, L. R. Qian, M. J. Li, H. J. Li, X. C. Niu and B. H. Yang, *Mater. Today Commun.*, 2019, **21**, 100680.
15 P. R. Chikate, P. K. Bankar, R. J. Choudhary, Y. R. Ma, S. I. Patil, M. A. More, D. M. Phase, P. M. Shirage and R. S. Devan, *RSC Adv.*, 2018, **8**, 21664–21670.
16 P. R. Chikate, K. D. Daware, D. S. Gayhane, Y. R. Ma, R. J. Choudhary, S. I. Patil, M. A. More, D. M. Phase, S. W. Gosavi, P. M. Shirage and R. S. Devan, *ChemistrySelect*, 2018, **3**, 7891–7899.
17 P. R. Chikate, K. D. Daware, S. S. Patil, P. N. Didwal, G. S. Lole, R. J. Choudhary, S. W. Gosavi and R. S. Devan, *New J. Chem.*, 2020, **44**, 5535–5544.
18 Y. Cai and H. Q. Fan, *CrystEngComm*, 2013, **15**, 9148–9153.
19 P. Patil, G. Gaikwad, D. R. Patil and J. Naik, *Bull. Mater. Sci.*, 2016, **39**, 655–665.
20 N. Caicedo, R. Leturcq, J. P. Raskin, D. Flandre and D. Lenoble, *Sens. Actuators, B*, 2019, **297**, 126602.
21 P. Rai, W. K. Kwak and Y. T. Yu, *ACS Appl. Mater. Interfaces*, 2013, **5**, 3026–3032.
22 D. W. Wang, S. S. Du, X. Zhou, B. Wang, J. Ma, P. Sun, Y. F. Sun and G. Y. Lu, *CrystEngComm*, 2013, **15**, 7438–7442.
23 S. J. Chang, W. Y. Weng, C. L. Hsu and T. J. Hsueh, *Nano Commun. Netw.*, 2010, **1**, 283–288.
24 H. Colak and E. Karakose, *Sens. Actuators, B*, 2019, **296**, 126629.
25 K. M. Kim, H. R. Kim, K. I. Choi, H. J. Kim and J. H. Lee, *Sens. Actuators, B*, 2011, **155**, 745–751.
26 A. Sharma, P. Bhojane, A. K. Rana, Y. Kumar and P. M. Shirage, *Scr. Mater.*, 2017, **128**, 65–68.
27 S. Kanaparthi and S. G. Singh, *Mater. Sci. Energy Technol.*, 2020, **3**, 91–96.
28 G. Kresse, J. Furthmüller and J. Hafner, *Phys. Rev. B: Condens. Matter Mater. Phys.*, 1994, **50**, 13181–13185.
29 P. E. Blöchl, *Phys. Rev. B: Condens. Matter Mater. Phys.*, 1994, **50**, 17953–17979.
30 J. P. Perdew, K. Burke and M. Ernzerhof, *Phys. Rev. Lett.*, 1997, **78**, 1396.
31 S. Grimme, J. Antony, S. Ehrlich and H. A. Krieg, *J. Chem. Phys.*, 2010, **132**, 19.
32 A. V. Krukau, O. A. Vydrov, A. F. Izmaylov and G. E. Scuseria, *J. Chem. Phys.*, 2006, **125**, 224106.

33 G. Mattioli, F. Filippone, P. Alippi, P. Giannozzi and A. A. Bonapasta, *J. Mater. Chem.*, 2012, **22**, 440–446.
34 D. J. Cooke, A. Marmier and S. C. Parker, *J. Phys. Chem. B*, 2006, **110**, 7985–7991.
35 G. W. Watson, E. T. Kelsey, N. H. de Leeuw, D. J. Harris and S. C. Parker, *J. Chem. Soc., Faraday Trans.*, 1996, **92**, 433–438.
36 P. W. Tasker, *J. Phys. C: Solid State Phys.*, 1979, **12**, 4977.
37 W. Tang, E. Sanville and G. A. Henkelman, *J. Phys.: Condens. Matter*, 2009, **21**, 084204.
38 C. Y. Geng, Y. Jiang, Y. Yao, X. M. Meng, J. A. Zapien, C. S. Lee, Y. Lifshitz and S. T. Lee, *Adv. Funct. Mater.*, 2004, **14**, 589–594.
39 Z. W. Dong, C. F. Zhang, H. Deng, G. J. You and S. X. Qian, *Mater. Chem. Phys.*, 2006, **99**, 160–163.
40 R. Cusco, E. Alarcon-Llado, J. Ibanez, L. Artus, J. Jimenez, B. G. Wang and M. J. Callahan, *Phys. Rev. B: Condens. Matter Mater. Phys.*, 2007, **75**, 165202.
41 A. G. Milekhin, N. A. Yeryukov, L. L. Sveshnikova, T. A. Duda, C. Himcinschi, E. I. Zenkevich and D. R. T. Zahn, *Appl. Phys. A: Mater. Sci. Process.*, 2012, **107**, 275–278.
42 S. S. Lo and D. S. Huang, *Langmuir*, 2010, **26**, 6762–6766.
43 Q. Simon, D. Barreca, A. Gasparotto, C. Maccato, E. Tondello, C. Sada, E. Comini, A. Devi and R. A. Fischer, *Nanotechnology*, 2012, **23**, 025502.
44 L. W. Wang, Y. F. Kang, X. H. Liu, S. M. Zhang, W. P. Huang and S. R. Wang, *Sens. Actuators, B*, 2012, **162**, 237–243.
45 J. Guo, J. Zhang, M. Zhu, D. X. Ju, H. Y. Xu and B. Q. Cao, *Sens. Actuators, B*, 2014, **199**, 339–345.
46 Z. X. Yang, Y. Huang, G. Chen, Z. P. Guo, S. Y. Cheng and S. Z. Huang, *Sens. Actuators, B*, 2009, **140**, 549–556.
47 T. Tharsika, M. Thanihaichelvan, A. Haseeb and S. A. Akbar, *Front. Mater.*, 2019, **6**, 122.
48 M. Shahabuddin, A. Sharma, J. Kumar, M. Tomar, A. Umar and V. Gupta, *Sens. Actuators, B*, 2014, **194**, 410–418.
49 C. F. Li, C. Y. Hsu and Y. Y. Li, *J. Alloys Compd.*, 2014, **606**, 27–31.
50 J. H. Kim, A. Mirzaei, H. W. Kim and S. S. Kim, *ACS Appl. Mater. Interfaces*, 2019, **11**, 24172–24183.
51 P. K. Baviskar, S. R. Rondiya, G. P. Patil, B. R. Sankapal, H. M. Pathan, P. G. Chavan and N. Y. Dzade, *ACS Omega*, 2020, **5**, 6715–6724.
52 D. Zappa, E. Comini and G. Sberveglieri, *Nanotechnology*, 2013, **24**, 444008.
53 C. F. Li, C. Y. Hsu and Y. Y. Li, *J. Alloys Compd.*, 2014, **606**, 27–31.

